

Spin-up of a superfluid vortex lattice driven by rough boundaries


N. A. Keepfer*

*Joint Quantum Centre (JQC) Durham-Newcastle, School of Mathematics, Statistics and Physics, Newcastle University,
Newcastle upon Tyne, NE1 7RU, United Kingdom*

and INO-CNR BEC Center, Dipartimento di Fisica, Universit di Trento, Via Sommarive 14, I-38123 Trento, Italy

G. W. Stagg, L. Galantucci[✉], C. F. Barenghi, and N. G. Parker

*Joint Quantum Centre (JQC) Durham-Newcastle, School of Mathematics, Statistics and Physics, Newcastle University,
Newcastle upon Tyne, NE1 7RU, United Kingdom*

 (Received 1 May 2020; accepted 6 October 2020; published 21 October 2020)

We study numerically the formation of a vortex lattice inside a rotating bucket containing superfluid helium, paying attention to an important feature which is practically unavoidable in all experiments: the microscopic roughness of the bucket’s surface. We model this using the Gross-Pitaevskii equation for a weakly interacting Bose gas, a model which is idealized when applied to superfluid helium but captures the key physics of the vortex dynamics which we are interested in. We find that the vortex lattice arises from the interaction and reconnections of nucleated U-shaped vortex lines, which merge and align along the axis of rotation. We quantify the effects which the surface roughness and remanent vortex lines play in this process.

DOI: [10.1103/PhysRevB.102.144520](https://doi.org/10.1103/PhysRevB.102.144520)

I. INTRODUCTION

Superfluids are extraordinary fluids characterized by the absence of viscosity. They are irrotational everywhere except at vortex lines whose circulation is quantized in units of $\kappa = h/m$, where h is Planck’s constant and m is the mass of the boson which composes the fluid [1,2]. First discovered and studied in liquid helium-4 and, decades later, in helium-3, superfluidity has since been observed in ultracold gases and photonic systems. The constraint of quantized vorticity is a consequence of quantum mechanics—vorticity can only arise as 2π topological defects of the macroscopic single-particle wave function of the quantum many-body system. These defects manifest as vortex lines through the fluid. As well as possessing a circulating flow, the vortex lines have a core of depleted density about their axis, out to a core radius a_0 which is of the order of the superfluid healing length. In helium-4 and helium-3 the vortex core size is around 10^{-10}m and 10^{-8}m , respectively.

The textbook paradigm of superfluidity is a cylindrical bucket of superfluid helium rotating at constant angular frequency Ω . Classical solid-body rotation is forbidden by the irrotational nature of the superfluid. At sufficiently small values of Ω , the fluid remains quiescent. However, if Ω is increased past a critical value Ω_c , the presence of a vortex line is energetically favorable. Using hydrodynamic arguments and up to a logarithmic correction, it is estimated [2] that this critical angular frequency is

$$\Omega_c = \frac{\hbar}{mR^2} \ln \left(\frac{R}{a_0} \right), \quad (1)$$

where m is the mass of a helium atom and R is the radius of the bucket. At larger values of Ω , two vortices become favorable, and so on. For $\Omega \gg \Omega_c$ the stationary state of the fluid is the famed vortex lattice, an array of vortex lines aligned along the axis of rotation with areal density,

$$n_v = \frac{2\Omega}{\kappa}, \quad (2)$$

known as Feynman’s rule. The vortex lattice was first imaged in superfluid helium by Packard *et al.* [3] and more recently by Bewley *et al.* [4]. The lattice has also been observed in ultracold gaseous superfluids trapped by smooth confining potentials [5,6]. (At much higher rotation frequencies where centrifugal effects dominate, a giant or macroscopic vortex carrying many quanta of circulation can become formed in both superfluid helium [7,8] and gaseous superfluids [9–12]; however, this regime is outside the scope of this work).

The process in which the vortices enter the superfluid in the first place is called vortex nucleation. Being associated with a 2π phase singularity of the macroscopic wave function, a vortex line is topologically protected. Thus, starting from some initially vortex-free state, vortices must enter the superfluid from the boundary. It is believed that vortex lines are nucleated either *intrinsically* by the flow of the superfluid past the microscopic roughness of the bucket wall (overcoming a critical velocity) or *extrinsically* by stretching some pre-existing vortex lines called “remanent vortices” which, under suitable conditions, can spool additional vortices [13]. Remanent vortices are thought to arise when cooling the helium sample through the superfluid transition, and can be avoided by using careful experimental protocols [14].

Individual vortex nucleation in a rotating bucket, either intrinsic or extrinsic, has never been visualized in detail.

*n.a.l.keepfer1@ncl.ac.uk

Experimentally, it remains challenging to image the flow in the vicinity of a boundary, despite progress in flow visualization in the bulk [4,15,16], more so because the microscopic scale of the vortices themselves. Theoretically, the nucleation problem has been addressed using energy arguments [17,18] with no insight in the dynamics. With few exceptions [19], the effect of microscopic boundary roughness on the vortex nucleation has not been studied. A related and better understood nucleation process takes place when an ion bubble is driven in liquid helium by an applied electric field; compared to the bucket, the nucleation is more controlled in terms of geometry (the shape of the bubble can be determined theoretically) and velocity (experimentally determined by time of flight measurements). Vortex nucleation by the ion bubble has thus received much detailed experimental and theoretical attention [20–24] than nucleation by the walls of the bucket which contains the helium sample.

In this work we are not concerned with the vortex nucleation as such, but rather with the intermediate state between the nucleation and the final vortex lattice. This intermediate stage is still unexplored, but, given that the length scales and the time scales involved depend on the vortex separation rather than the vortex core size (i.e., they are mesoscopic rather than microscopic), there is the prospect of experimental visualization in the near future. The focus of attention is therefore not individual vortex dynamics at nucleation but the collective dynamics of many vortex lines in the presence of a boundary which is not smooth. For simplicity we consider the problem at sufficiently low temperature that the normal fluid does not play an important role.

The traditional method to model the dynamics of superfluid vortices is the vortex filament method (VFM) [25], which models vortex lines as infinitesimally thin filaments interacting with themselves, their neighbors and the boundary (via suitable images). However, this approach is not applicable to our problem. First, if the boundary varies on atomic length scales comparable to the vortex core (which is likely to be the case for any metal or glass bucket containing liquid helium), then the core length scale can no longer be ignored compared to other relevant length scale, invalidating the assumptions behind the VFM. Second, the implementation of the boundary condition is cumbersome to set up and not simple to change from one boundary shape to another; indeed, the VFM has been implemented for plane [26], semispherical [26,27], spherical [28,29], and cylindrical [30,31] boundaries, but never for irregular boundaries relevant to our problem. Third, the VFM does not describe vortex nucleation, but requires one to initialize the calculation with arbitrary seeding vortex lines. An alternative approach is through the Gross-Pitaevskii equation (GPE) [2,32]. This is a formal description of a dilute weakly interacting gas of bosons, and is equivalent to a continuity equation and an Euler-like equation for an inviscid fluid (the modification being the presence of a quantum pressure term). While the GPE is an excellent quantitative description of Bose gas superfluids, it is limited to being a qualitative description of superfluid helium due to the stronger interactions taking place in a liquid rather than in a gas. Nevertheless, its capability to describe the microscopic detail of superfluid dynamics—the finite-sized core, vortex interactions, and reconnections, even the intrinsic nucleation—makes it a useful

model to study superfluid flows at a boundary. An important feature is that the GPE can easily implement irregular boundaries. Indeed, recent GPE simulations have predicted the occurrence of a turbulent boundary layer when the superfluid flows past a locally rough surface [19]: above a critical imposed flow speed, vortices are nucleated from the surface features, interact, and become entwined in a layer adjacent to the surface.

Returning to the rotating bucket of superfluid helium, it is natural to ask if some kind of boundary layer may similarly form at the boundary of the rotating bucket in the transient evolution to the vortex lattice. Whether disordered or laminar, this layer will certainly involve vortex interactions. It is in fact unlikely that the vortex lines which nucleate extend from the top to the bottom of the bucket, as if the process were essentially two-dimensional (2D). More likely, the first vortex lines which nucleate are small, and become long only after a sequence of interactions and reconnections. To qualitatively explore these interactions, here we perform a series of numerical experiments, based on the GPE, of a superfluid being spun-up in a bucket whose walls are microscopically rough. These numerical experiments allows us to build a physical picture of how vorticity enters the superfluid and forms a vortex lattice, and of the role of remanent vortices, sharp intrusions, rotation rate, and dimensionality.

The plan of the paper is the following. In Sec. II we introduce our model and details our of numerical simulations. In Sec. III we present our main results for the spin-up of a quiescent superfluid. Section IV explores the possibility that a single strong imperfection in the shape of a protuberance, remanent vortex lines, or dimensionality may affect the main results described in Sec. III. Finally, in Sec. V we discuss and conclude our findings.

II. MODEL AND METHOD

A. Gross-Pitaevskii equation

We model the superfluid dynamics using the Gross-Pitaevskii equation. Within this model, the superfluid is parametrized by a mean-field complex wave function $\Psi(\mathbf{r}, t) = |\Psi(\mathbf{r}, t)|e^{iS(\mathbf{r}, t)}$. The particle density follows as $n(\mathbf{r}, t) = |\Psi(\mathbf{r}, t)|^2$ and the fluid velocity as $\mathbf{v}(\mathbf{r}, t) = (\hbar/m)\nabla S(\mathbf{r}, t)$, where $\hbar = h/(2\pi)$ and $S(\mathbf{r}, t)$ is the phase distribution of Ψ . The dynamics of $\Psi(\mathbf{r}, t)$ follows the GPE [2,32],

$$i\hbar\frac{\partial\Psi}{\partial t} = \hat{\mathcal{H}}\Psi, \quad (3)$$

with Hamiltonian operator,

$$\hat{\mathcal{H}} = -\frac{\hbar^2}{2m}\nabla^2 + V + g|\Psi|^2. \quad (4)$$

Here m is the particle mass, $g(>0)$ is a nonlinear coefficient describing the interparticle interactions, and $V(\mathbf{r}, t)$ is the external potential acting on the fluid. Stationary solutions of the GPE satisfy $\hat{\mathcal{H}}\Psi = \mu_0\Psi$, where μ_0 is the chemical potential of the fluid.

We make two physically motivated modifications to the basic GPE above. First, since the GPE conserves energy, we follow other works [33,34] in introducing a phenomenological

dissipation term into the GPE to model, at least in a qualitative way, the damping of excitations of the superfluid (for example, by their interaction with the normal fluid). This is achieved by replacing the left side of Eq. (3) with $(i - \gamma)\hbar \partial \Psi / \partial t$, where γ specifies the strength of the dissipation. Although not as accurate the friction included within the VFM, this phenomenological dissipation will help damp out the oscillations of the vortex lines (Kelvin waves), which is the main effect of the friction which concerns us here. Second, given our rotating scenario, we work in the reference frame rotating at constant angular frequency Ω about the z axis; this is achieved by modifying the GPE Hamiltonian to $\hat{\mathcal{H}} - i\Omega L_z$, where L_z is the angular momentum operator about z . In Cartesian coordinates $L_z = i\hbar(y\partial_x - x\partial_y)$.

B. Bucket setup

We consider the fluid to be confined within a cylindrical bucket of radius R and height H . The axis of the cylinder is the z axis of rotation. The bucket is modeled through the potential $V(\mathbf{r})$: In the interior of the bucket we set $V = 0$ while at the boundary and beyond we set $V \gg \mu_0$. In the ground state, the fluid density has the bulk value n_0 in the center of the bucket, while close to the bucket wall it heals to zero density over a length scale characterized by the healing length $\xi = \hbar / \sqrt{mn_0g}$. The healing length also characterizes the size of the cores of vortices in the fluid. Note that the chemical potential in the bulk is $\mu_0 = n_0g$. The speed of sound in the uniform systems is $c = \sqrt{n_0g/m}$.

It is clearly computationally impossible to simulate the range of length scales which are realistic for a typical experiment with liquid helium in the context of the GPE model. The dimensions (radius and height) of typical buckets used in the experiments are of the order of the centimeter, which is around eight orders of magnitude larger than the vortex core size in helium-4, $a_0 = 10^{-10}\text{m}$ (in helium-3 the vortex core is about 100 times larger). Instead, in our numerical experiments we employ buckets whose scale is around two orders of magnitude larger than the vortex core size. While this is clearly a vast scale reduction compared to real systems, the separation of scales between the vortices and the bucket size is sufficient to give us a qualitative insight into the dynamics of the vortex lines.

C. Surface roughness

To mimic the experimentally unavoidable surface roughness, we modify the azimuthal face of the bucket away from a perfect cylindrical shape using a noisy two-dimensional (2D) function. This function is numerically generated through a two-dimensional fractal Brownian motion [35] with Hurst index of 0.3, a parameter which describes the fractal dimension of the surface [36]. The choice to model the roughness in this way is motivated by the well-established fractal properties of real surfaces, including machined surfaces (of relevance to helium experiments), and the success of fractal Brownian motion in modeling a wide variety of real rough surfaces [37]. The function is normalized between 0 and 1, and is mirrored about its edge and recombined with itself in order to create periodicity across one dimension; a single realization of the

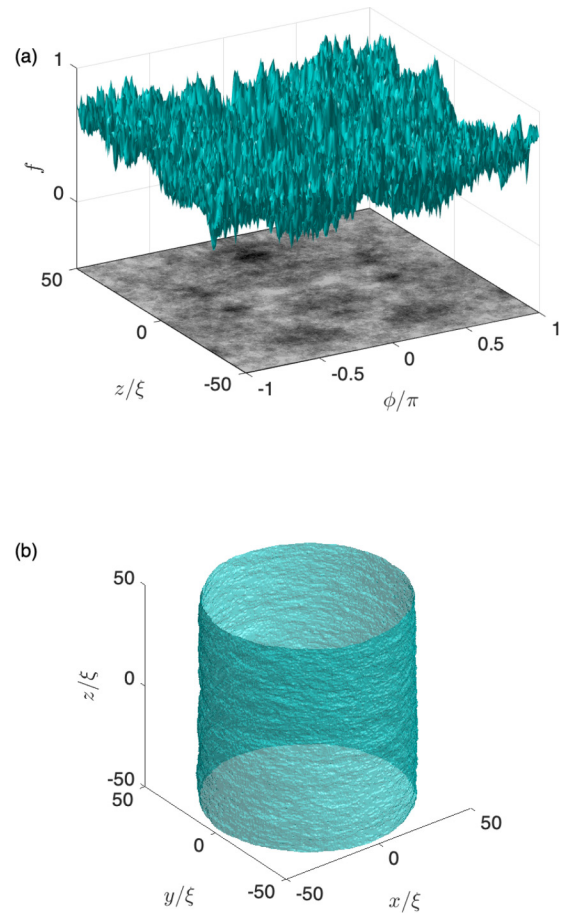


FIG. 1. (a) An example of the 2D fractional Brownian motion function f , normalized to the range $[0,1]$, shown as a surface plot and a heat map. (b) The rough cylindrical boundary of our bucket is formed by using the surface in (a) to modulate the radius of the bucket boundary with an amplitude a . Here $a = 0.1$.

function is depicted in Fig. 1(a). The function is mapped onto the space of axial coordinate z and azimuthal angle θ , and used to modify the radius of the bucket according to the form,

$$r(z, \phi) = R(1 - af(z, \theta)), \quad (5)$$

where R is the smooth bucket radius and a is the (dimensionless) roughness parameter. This numerical procedure generates all of our rough three-dimensional (3D) bucket shapes. By computing the local curvature of the surface roughness, we find that the values of the average radius of curvature corresponding to values $a = 0.05, 0.1, 0.2,$ and 0.3 of the roughness parameter are $10.4\xi, 5.2\xi, 2.6\xi,$ and 1.7ξ , respectively (small values of a correspond to large radius of curvature, i.e., smoother surface). For simplicity, the top and bottom surfaces of the bucket are left smooth. The reason is that, by providing the vortex lines with pinning sites, any roughness on these surfaces will act essentially as an extra friction (an effect which is already qualitatively accounted for via the dissipation parameter γ) slowing down the final stage of crystallization of the vortex lattice.

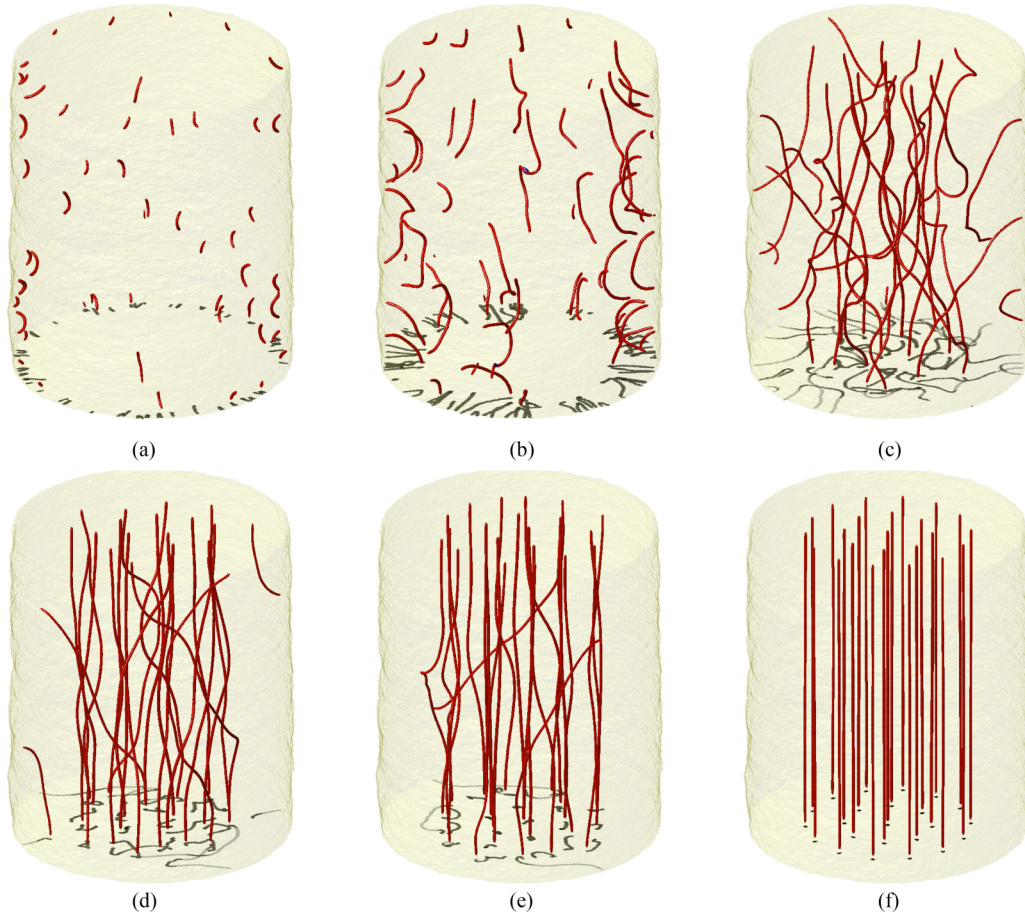


FIG. 2. Three-dimensional snapshots at times $t/\tau = 100$ (a), 200 (b), 500 (c), 1000 (d), 1500 (e), and 3000 (f) during the spin-up of the initially quiescent fluid. The vortex cores are identified by density isosurfaces; vortices with positive and negative circulation (as determined by their pseudovorticity [39] in the z direction) are visualized in red and blue, respectively. The faint yellow isosurface represents the confining bucket. A false-color shadow is projected onto the bottom surface to enhance the visualization of the 3D vortex lines.

D. Simulation setup

The initial condition for Ψ in all of our simulations is the nonrotating ground-state solution, found by the method of imaginary time propagation of the GPE, supplemented with low-amplitude white noise to Ψ (amplitude 0.001) to break any symmetries artificially presented in the initial condition. We then impose a constant rotation on the system for $t > 0$, with fixed rotation frequency Ω . Note that Ω far exceeds the critical rotation frequency to support vortices Ω_c , such that the lowest energy state of the fluid is a vortex lattice.

The nondimensionalization of the GPE is based on the natural units of the homogeneous fluid [2]: The unit of length is the healing length ξ , the unit of speed is c , the unit of time is $\tau = \xi/c = \hbar/\mu_0$, the unit of energy is μ_0 , and the unit of density is n_0 . Both our 3D and 2D numerical simulations are performed using XMD52 [38], an open-source partial and ordinary differential equation solver. The time evolution of the dimensionless GPE is computed via an adaptive fourth-fifth-order Runge-Kutta integration scheme with typical time step $dt = 0.01\tau$ and grid spacing $dx = 0.4\xi$; these discretization numbers are sufficiently small to resolve the smallest spatial features (vortices and the fluid boundary layer, which are of the order of a few healing lengths) and

the shortest time scales in the fluid. We typically conduct our 3D simulations on a cubic grid of size 256^3 . Threaded parallel processing is employed using the OPENMP standard across typically 44 threads to improve processing speeds on computationally intensive simulations.

III. RESULTS

A. Typical spin-up dynamics

We now demonstrate the typical spin-up of an initially quiescent fluid. Unless otherwise indicated, we present results for the following choice of parameters: bucket radius $R = 50\xi$, bucket height $H = 100\xi$, rotation frequency $\Omega = 0.02\tau^{-1}$, dissipation parameter $\gamma = 0.05$, and roughness parameter $a = 0.1$ (meaning that the irregular surface of the bucket extends radially from 45ξ to 50ξ , corresponding to irregular “surface bumps” of height up to five healing lengths).

The evolution of the fluid is illustrated by the snapshots shown in Fig. 2 in which the vortex lines are tracked in 3D space using a precise method introduced in Ref. [39]; movies of the evolution are available in Supplemental Material [40]. From the initial quiescent and vortex-free fluid, first we see the nucleation of vortex lines at the cylindrical boundary of

the fluid [Fig. 2(a)]. These vortices are all singly quantized; we do not detect the presence of multiply charged vortices in any of our simulations, which is consistent with the energetic instability of multiply charged vortices and the favorability of singly charged vortices [2]. The nucleation takes place at the sharpest features on the surface, as seen in a previous calculation over a flat rough surface [19]: At these features the local (potential) flow velocity is raised by the curvature of the boundary, and exceeds the critical velocity of vortex nucleation, which, according to Landau's criterion, in a Bose gas is $v_c \approx c$. Since the local flow speed around a moving obstacle always exceeds the translational speed of the obstacle, Landau's criterion can be satisfied by a translational speed less than c . For example, a cylindrical obstacle moving at speed approximately equal to $0.4c$ will nucleate vortices [41,42]. In our case ($\Omega = 0.02/\tau$ and $R = 50\xi$), the translational speed of the prominences on the rough boundary is approximately $\Omega R \approx c$, which is sufficient to exceed Landau's criterion and nucleate vortices. Figures 2(a) and 2(b) show that the vortex lines which nucleate at the rough boundary have the shape of small half-loops or handles; similar vortex shapes have been reported in trapped Bose-Einstein condensates [43] and turbulent superfluid helium-4 near a heated cylinder [44], and have been called, respectively, "U vortices" and "handles."

We next consider the angular momentum of the fluid, exploring its evolution and distribution. We define the density of the z component of the angular momentum of the fluid as

$$L_z(x, y, z) = \psi^* i\hbar \left(y \frac{\partial}{\partial x} - x \frac{\partial}{\partial y} \right) \psi. \quad (6)$$

Figure 3(a) shows the angular momentum density as a function of the radial coordinate, averaged vertically and azimuthally, $\langle L_z \rangle$. At $t = 0$, this is zero throughout the fluid. As time evolves, angular momentum builds at the edge of the bucket and drifts inwards, corresponding to the nucleation and inward drift of the vortex lines. At steady state, the angular momentum forms a stepped curve, with each step corresponding to a concentric ring of vortex lines in the final lattice. Note how the final distribution of the angular momentum approximately follows the result of solid-body rotation with constant mass density, $mn_0\Omega r^2$. The total z component of the angular momentum $\mathcal{L} = \iiint L_z dx dy dz$ [inset in Fig. 3(a)] grows in time, saturating at a final value by around $t \sim 2000 \tau$, which is when the vortex lines have settled into the lattice configuration. In gaseous superfluids confined within smooth potentials, recent results of merging superfluids [45,46] suggest that the rate of angular momentum transfer between a static and rotating state is constant; however, here the growth of the angular momentum follows a sigmoidal curve, rather than a linear one.

We also consider the distribution of the vortex length projected in the z direction, Λ_z , as a function of radius, shown in Fig. 3(b). At early times, vortex length exists only near the bucket edge, spreading progressively into the bulk. Later, the vortex length converges towards falling at discrete peaks at $r = 0$, $r \approx 13\xi$ and $r \approx 26\xi$, corresponding to the concentric arrangement of vortices in the lattice configuration.

The collection of U vortices nucleated at the boundary is the superfluid's analog of a boundary layer, the region separating the rotating boundary from the still quiescent bulk of the

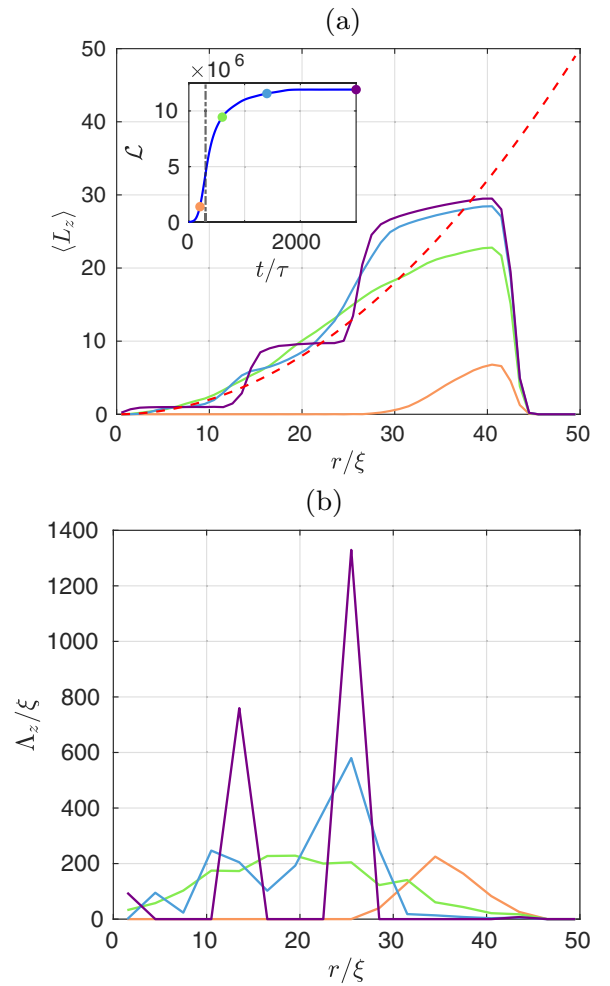


FIG. 3. (a) Angular momentum density as a function of radius at various times during the spin-up of the rough bucket (same parameters as in Fig. 2). Plotted is the angular momentum density averaged over the z dimension $\langle L_z \rangle$. The lines correspond to times indicated by circular markers on the inset. The distribution of the angular momentum of a solid body of uniform density is shown by the red dashed line. The inset shows the evolution of the total angular momentum of the fluid $\mathcal{L} = \iiint L_z dx dy dz$. (b) The vortex length projected in the z direction Λ_z plotted as a function of radius, at the same times as in (a). The data is binned in radial intervals of 3ξ .

fluid. The U vortices tend to be aligned along the z direction, creating a superflow in the same direction of the rotating boundary. The vortex nucleation is therefore short-lived, since the nucleated U vortices reduce the relative motion between the fluid and the boundary, suppressing further nucleations. In time, the U vortices grow in size and extend further into the fluid [Figs. 2(b) and 2(c)], ultimately filling the bulk [Fig. 2(d)]. During this stage of the evolution, the U vortices also grow in vertical extent in the z direction, occasionally connecting and merging with each other, thus increasing their vertical extent. When the length in the z direction becomes of the order of the bucket's height H , one or both vortex endpoints start sliding along the smooth top and/or bottom of the bucket. Once most of the vortex lines are fully extended from the top to the bottom of the bucket, they quickly drift

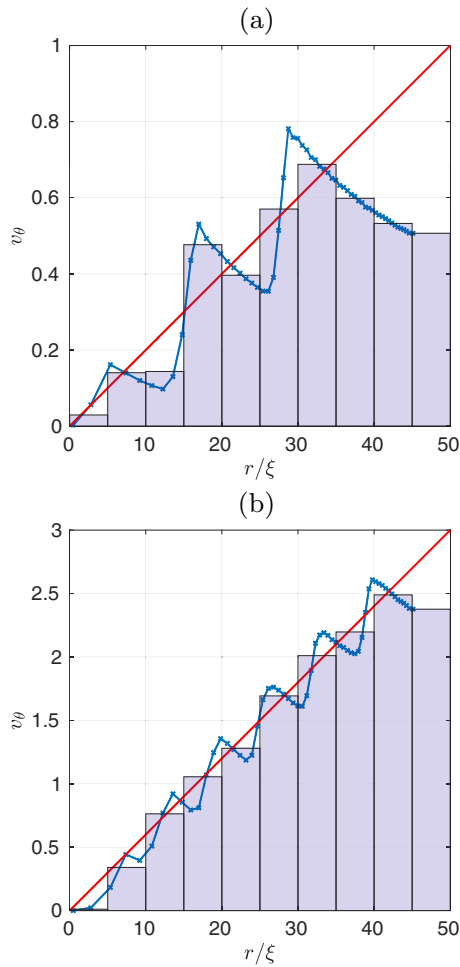


FIG. 4. Azimuthal velocity v_θ of the fluid as a function of radius r , for rotation frequencies of $\Omega = 0.02 \tau^{-1}$ (a) and $\Omega = 0.06 \tau^{-1}$ (b). We use roughness parameter $a = 0.1$. The solid red lines represent solid-body rotation $v_\theta = \Omega r$; the blue lines are values of $v_\theta(r)$ averaged in the θ direction; the pale blue rectangles are histograms with bin size $\Delta r = 5\xi$ (therefore the outer bins contain more data points). It is apparent that the more rapid rotation (b) creates a vortex lattice in better agreement with the solid-body rotation, and that there is a vortex-free region near the boundary.

into the bulk of the fluid. Although the vortex lines are aligned along the direction of rotation, they remain highly excited and undergo reconnection events when they collide with each other. Over time they relax towards a regular configuration of straight vortices. A small proportion of U vortices remain attached to the side of the bucket for a longer period of time [Fig. 2(d)]; over a longer time they detach, and relax to the final lattice configuration. Some of the vortex lines end up diagonally across the rest of the vortex lattice [Fig. 2(e)]: Eventually they also relax to the final lattice configuration [Fig. 2(f)]. The vortex lattice is stationary in the rotating frame, representing the lowest energy state of the rotating superfluid. In this final state, the coarse-grained fluid velocity approximates the solid-body result $\mathbf{v} = v_\theta \mathbf{e}_\theta = \Omega r \mathbf{e}_\theta$, where \mathbf{e}_θ is the azimuthal unit vector, as shown in Fig. 4; as expected, the agreement improves with increasing Ω , and there is a vortex-free region near the boundary.

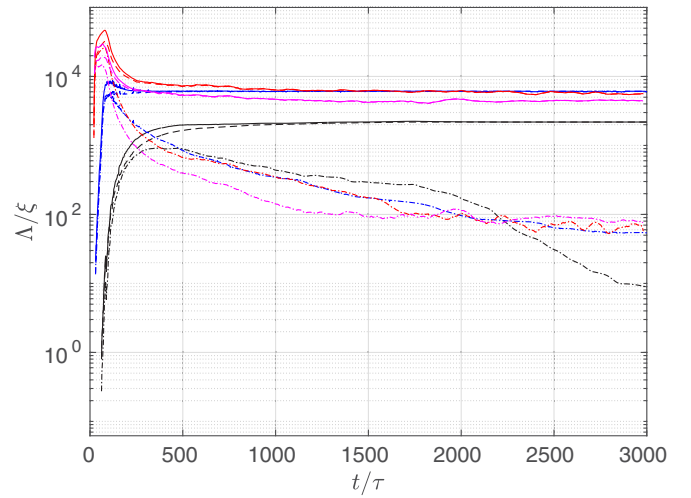


FIG. 5. Evolution of the total vortex length, Λ (solid lines), as well as the vortex length in the z direction Λ_z (dashed lines) and the vortex length in the xy plane Λ_{xy} (dot-dashed lines), plotted versus time t for different angular velocity of rotation $\Omega = 0.02 \tau^{-1}$ (black), $0.04 \tau^{-1}$ (blue), and $0.06 \tau^{-1}$ (red) achieving final values of the vortex length $\Lambda_\infty = 2184\xi$, 6007ξ , and 5568ξ , respectively. All curves refer to roughness parameter $a = 0.1$.

Our 3D results are presented for a fixed bucket size due to computational constraints of simulating a larger system. For a larger bucket we would expect qualitatively similar dynamics; indeed our 2D results in a larger bucket presented in Sec. IV C support this. The most significant change under a larger bucket is more vortices in the final state (at a fixed rotation frequency) and as a result a better approximation to solid-body rotation.

B. Role of angular velocity and roughness

To analyze the vortex dynamics further it is useful to distinguish the total vortex length Λ from the vortex length projected in the z direction Λ_z , and the vortex length projected in the xy plane Λ_{xy} . In the final vortex lattice all vortex lines are aligned along z , hence we expect that, after a sufficiently long time, $\Lambda_{xy} \approx 0$ and $\Lambda_z \approx \Lambda$, with $\Lambda \rightarrow N_v H$, where N_v is the final number of straight vortex lines. Figure 5 displays Λ (solid lines), Λ_z (dashed lines), and Λ_{xy} (dot-dashed lines) as a function of time for different angular velocities of rotation, $\Omega = 0.02, 0.04$, and 0.06 at the same roughness parameter $a = 0.1$. It is apparent that in the initial stage, a great amount of vorticity is in the xy plane, before realignment of the vortex lines along the z axis of rotation takes place. The effect is particularly noticeable at the largest angular velocities, for which, during the initial transient, the vortex length is considerably larger than the value Λ_∞ achieved in the final vortex lattice configuration. Moreover, we see that the final vortex line length increases with Ω due to the increasing number of vortices in the final state.

Figure 6 shows Λ , Λ_z , and Λ_{xy} plotted versus time at the same angular velocity $\Omega = 0.02 \tau^{-1}$ for different values of roughness parameter a . The largest values of the final vortex length Λ_∞ are achieved with $a = 0.1\xi$ and $a = 0.2\xi$. Smoother ($a = 0.05\xi$) and rougher ($a = 0.3\xi$) boundaries generate less vortex length. These variations in the final line

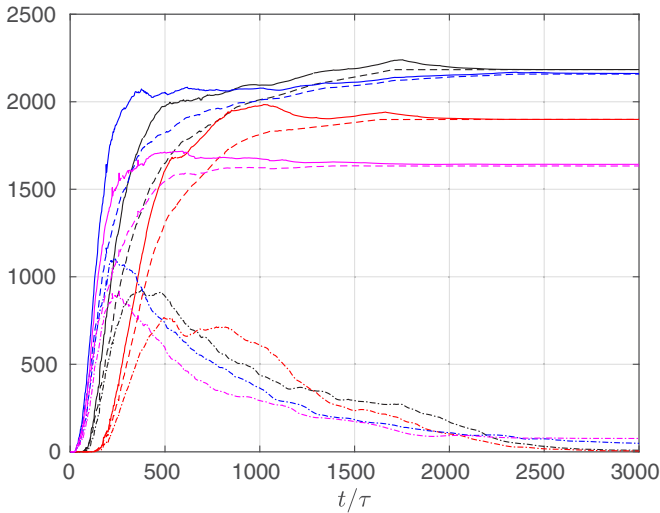


FIG. 6. Evolution of the total vortex length, Λ (solid lines), as well as the vortex length in the z direction Λ_z (dashed lines) and the vortex length in the xy plane Λ_{xy} (dot-dashed lines), plotted versus time t for different boundary roughness $a = 0.05$ (red), 0.1 (black), 0.2 (blue), and 0.3ξ (magenta), achieving final values $\Lambda_\infty = 1899 \xi$, 2184ξ , 2161ξ , and 1643ξ . All curves refer to the same angular velocity $\Omega = 0.02 \tau^{-1}$.

length arise to the final number of vortex lines varying by a few vortices across these cases. It is not surprising that the final vortex lattice depends on the roughness which has nucleated the initial vorticity. Feynman's rule [Eq. (2)] only refers to an idealized homogeneous system. Boundaries are known to have effects (e.g., missing vortex lines near the boundary) and it has been observed that the formation of the vortex lattice may be history dependent and involve metastability [47,48] and hysteresis [49].

Figure 7 compares the growth of angular momentum between the default case (blue line), the case where the rotation frequency is doubled (red line), and the case where the roughness amplitude is doubled (yellow line). The growth behavior is qualitatively similar in all cases. Doubling the rotation frequency leads to a much faster rate of injection of angular momentum, and a higher final value, consistent with the faster injection rate of vortex lines from the boundary and the higher density of vortex lines in the final lattice state. Doubling the surface roughness has little effect on the growth of the angular momentum, just slightly increasing the rate of angular momentum injection, which can be attributed to the greater injection rate of vortices from the rougher surface.

Figure 8 illustrates some of the final vortex patterns which we have computed by plotting the superfluid density, $|\psi(x, y)|^2$ in the xy plane at half-height of the bucket. In these pictures the vortices appear as small holes; to clarify the length scales, we recall that on the vortex axis the density is zero and that at distance $r = 2\xi$ from the axis, the density recovers about 80% of the bulk value at infinity. It is interesting to compare the different final vortex configurations for halved/doubled rotation velocity and the roughness parameter with respect to our default choice ($\Omega = 0.02 \tau^{-1}$ and $a = 0.1$). While the ideal 2D vortex lattice has a vortex at

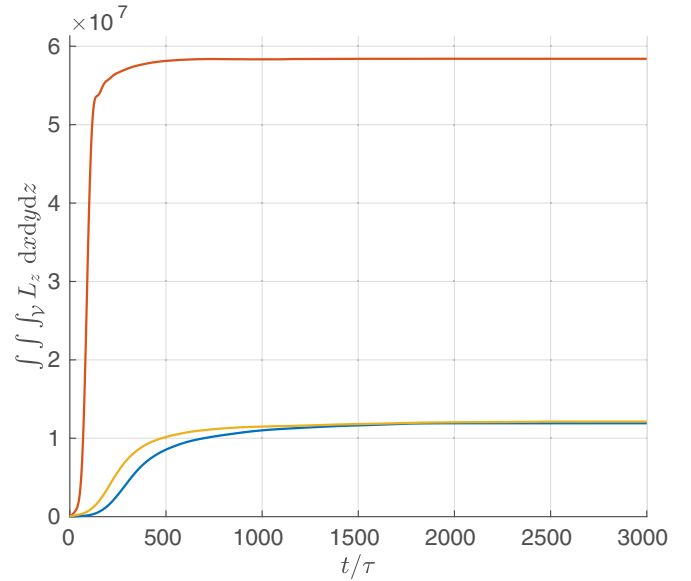


FIG. 7. Evolution of the total angular momentum for the default parameters used in Fig. 2 (blue line) double the rotation frequency (red line) and double the roughness amplitude (yellow line).

the center, surrounded by a first row of six vortices, a second row of 12 vortices, etc., the vortex configurations shown in Fig. 8 contain slightly different vortex numbers; in particular some configurations contain vortex lines which seem misplaced [Fig. 8(c)] or lack the vortex at the center [Fig. 8(e)]; these configurations are metastable states corresponding to local minima of the free energy in the rotating frame [47]. Moreover, at slow rotations [Figs. 8(a) and 8(d)] the predicted vortex-free region near the boundary [18,50,51] is clearly visible; this phenomenon affects the coarse-grained azimuthal velocity near the boundary shown previously in Fig. 4(a). The depletion of the background fluid density in the center of the bucket—particularly evident in Figs. 8(b) and 8(c)—is due to coarse-grained centrifugal effects, analogous to the classical rotating case [2].

IV. OTHER EFFECTS

In this section we repeat the simulation of Sec. III with several significant modifications: the presence of a single strong protuberance, the presence of remanent vortex lines, and the 2D case. The aim is to determine whether these effects change qualitatively the dynamics described in Sec. III.

A. Effect of a strong protuberance

First we consider the effect of a single strong imperfection in the form of a protuberance on the cylindrical wall. The question is whether, by enhancing vortex nucleation, the protuberance can induce a turbulent boundary layer. The protuberance is numerically created by adding a Gaussian-shaped potential to the existing (small-scale) roughness potential. Equation (5) is replaced by

$$r(z, \phi) = R[1 - a(f(z, \theta) + Gf_G(z, \theta))], \quad (7)$$

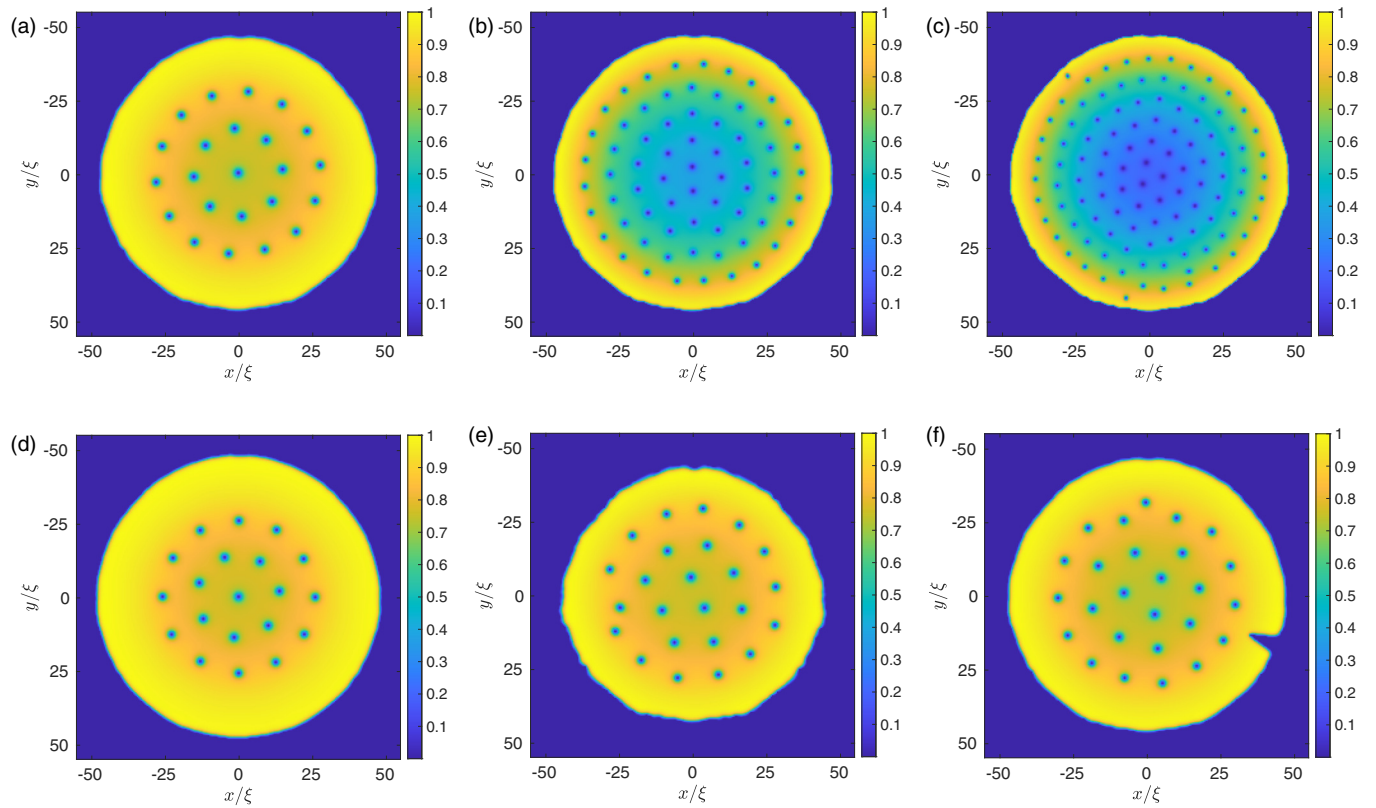


FIG. 8. Density profile in the xy plane at the half-height of the bucket, showing the final vortex configurations for the following cases: (a) $\Omega = 0.02 \tau^{-1}$ and $a = 0.1$ (default choice); (b) $\Omega = 0.04 \tau^{-1}$ and $a = 0.1$ (double rotation); (c) $\Omega = 0.06 \tau^{-1}$ and $a = 0.1$ (triple rotation); (d) $\Omega = 0.02 \tau^{-1}$ and $a = 0.05$ (half roughness); (e) $\Omega = 0.02 \tau^{-1}$ and $a = 0.2$ (double roughness); (f) $\Omega = 0.02 \tau^{-1}$ and $a = 0.1$ (single strong protuberance added; see Sec. IV).

where $G = 2$ and $f_G(z, \theta)$ is a Gaussian-shape function taking values from 0 to 1 and rms width 4ξ . The approximate height of the strong protuberance in the simulation which we present is 10ξ , as also visible in Fig. 8(f).

Snapshots taken during the time evolution for $\Omega = 0.02 \tau^{-1}$ and $a = 0.1$ are shown in Fig. 9; a movie can be viewed in Supplemental Material [52]. The protuberance catalyzes the local nucleation of vortices at early times: Large vortex loops (of the same size order as the protuberance) are

rapidly generated [Fig. 9(a)], leading to a downstream trail of loops [Figs. 9(b) and 9(c)], in addition to the slower nucleation of U vortices from the rough bucket wall. The vortex configuration becomes clearly anisotropic near the bucket edge [Fig. 9(d)]. However, once the vortices fill the bulk [Fig. 9(e)], memory of this effect is lost, and the subsequent evolution is very similar to the evolution without the strong protuberance. In fact, the final vortex lattice is not significantly different from the lattices considered in Sec. III, as shown in Fig. 8(f).

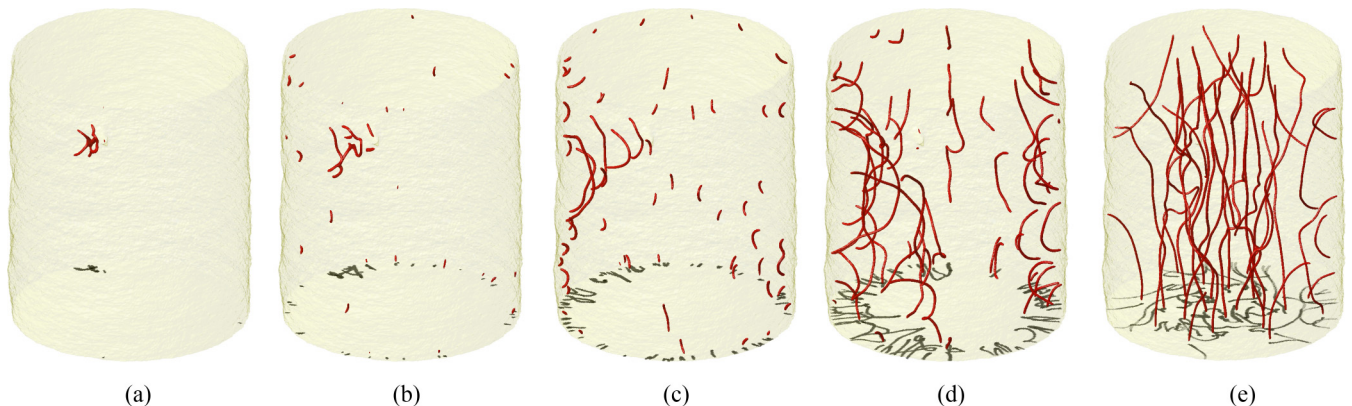


FIG. 9. Early-time dynamics during the spin-up of the fluid in the presence of a single strong protuberance added to the rough cylindrical boundary. The snapshots, taken at $t/\tau = 26, 50, 100, 200,$ and 500 , are presented in the same way as Fig. 2.

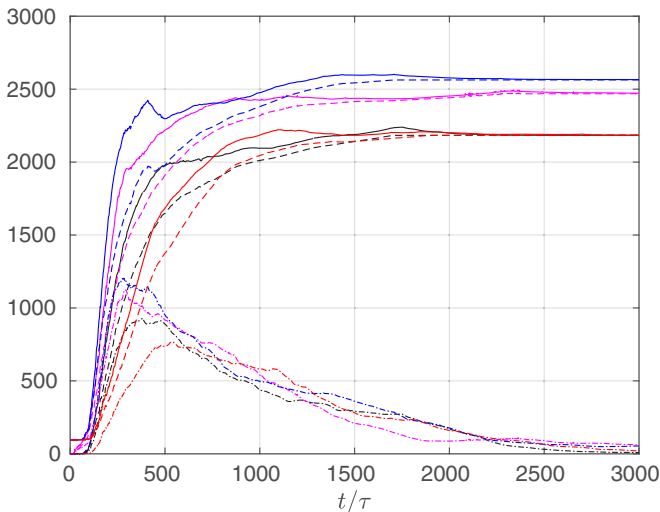


FIG. 10. Time evolution of Δ (solid line), Δ_z (dashed line), Δ_{xy} (dot-dashed line). The colors correspond to the simulations with default parameters $\Omega = 0.02\tau^{-1}$, $a = 0.1\xi$ (black), the added surface protuberance (magenta), the added remanent negative vortex (blue), and the added remanent positive vortex (red), respectively.

Figure 10 shows the time evolution of Δ , Δ_z , and Δ_{xy} in the presence of the protuberance (magenta lines) and its absence (black lines). This confirms that the protuberance accelerates the generation of vortex line length at early times, but that its effect becomes washed out at later times.

B. Effect of remanent vortices

Secondly, we consider the effect of remanent vortex lines. In experiments with liquid helium, it is believed that so-called “remanent vortices” may be present in the fluid, created via the Kibble-Zurek mechanism when cooling the helium sample through the superfluid transition to the final experimental temperature. The presence of remanent vortices may modify

the vortex nucleation and the formation of the vortex lattice when the sample is rotated. To explore this idea, we have repeated the simulations imposing a suitable phase profile to add a vortex to the initial state during the imaginary-time propagation. For simplicity we position the remanent vortex along the z axis of rotation.

The evolution of the superfluid with the standard rough cylindrical wall and a “positive” remanent vortex, that is, one whose circulation is oriented in the same direction of the bucket’s rotation is shown through Fig. 11 and the movie in Supplemental Material [53]. Compared to Sec. III, the only significant modification is a dampening of the initial injection of U vortices; the effect is visible by eye when comparing like-time snapshots [Figs. 2(b) and 11(a)]. The remanent vortex acts in the same direction as the rotating container: It reduces the relative speed between the bucket’s wall and the superfluid, and remains largely undisturbed at early times [Fig. 11(a)] until the U vortices that are nucleated fill the bulk and interact with it [Fig. 11(b)]; at this point the remanent vortex becomes subsumed within the other like-signed vortices [Fig. 11(c)], and the subsequent relaxation of the vortex configuration into a vortex lattice largely proceeds as if there was not any remanent vortex initially. Confirming this, we see that in Fig. 10 the presence of the positive vortex (red lines) depletes the generation of vortex line length at early times, but this recovers at later times such that the system reaches the same line length as in the absence of any remanent vortices (black lines).

If the remanent vortex is oriented in the direction opposite to the rotation of the bucket, i.e., a negative vortex, the evolution proceeds differently, as seen in Fig. 12 and the movie in Supplemental Material [54]. The remanent vortex enhances the nucleation of U vortices from the boundary, as evident from comparing Figs. 2(b) and 12(a). This effect is caused by the counterflow induced by the remanent vortex, which increases the relative speed of the fluid over the rough boundary. Once the other vortices drift close to the remanent vortex, the remanent vortex becomes excited by their

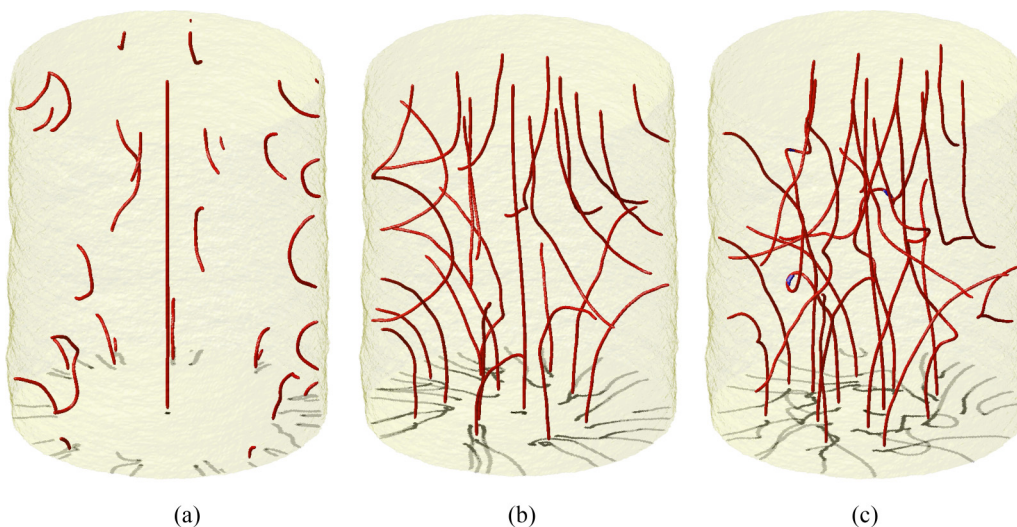


FIG. 11. Spin-up of the superfluid in the presence of a positively charged remanent vortex. Snapshots are taken at $t/\tau = 200, 400,$ and 500 , and are presented in the same way as Fig. 2.

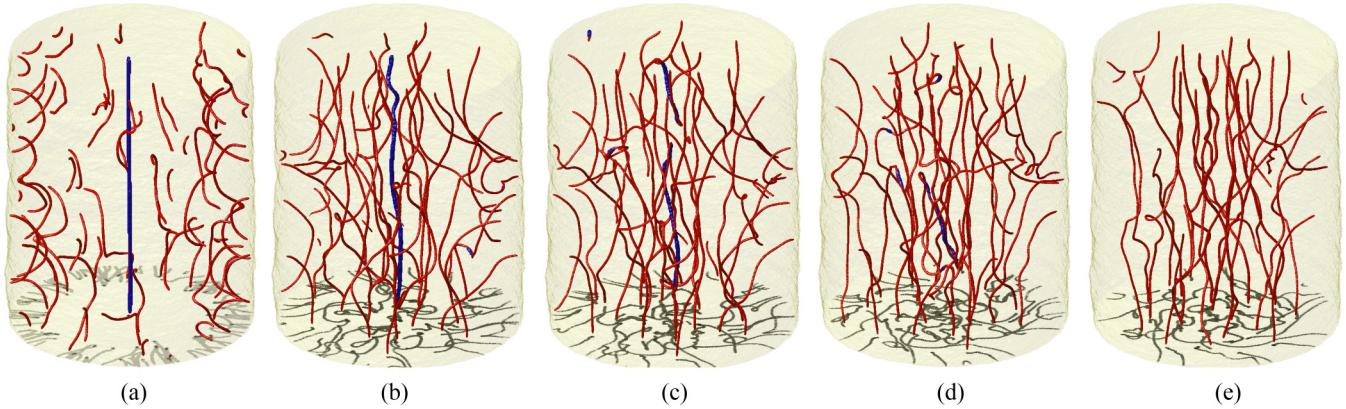


FIG. 12. Spin-up of the superfluid in the presence of a negatively charged remanent vortex. Snapshots are taken at $t/\tau = 200$ (a), 360 (b), 386 (c), 420 (d), and 500 (e). The images are presented in the same way as Fig. 2. Vortices with negative circulation are colored blue.

interaction [Fig. 12(b)]. A series of vortex reconnections break up the remanent vortex, forming progressively smaller vortex loops [Figs. 12(c) and 12(d)]. This leads to the rapid removal of vorticity of the “wrong” sign from the fluid [Fig. 12(e)]. Hereafter the fluid evolves in a similar manner to when the remanent vortex is absent [Sec. III], albeit with a slightly higher final vortex line length [Fig. 10].

C. 2D case

Finally, we have also performed the corresponding 2D simulations of the spin-up of a 2D superfluid within a rough circular boundary; the boundary is taken from the central slice of the 3D rough bucket. A movie showing the typical dynamics is available in Supplemental Material [55]. The 2D geometry allows calculations of much larger buckets, up to $R = 200\xi$ with a 1024^2 numerical grid. We observe the same qualitative behavior as in 3D in smaller buckets, albeit with many more vortices and without 3D effects such as vortex reconnections. Collisions of vortices of the opposite circulation result in the annihilation of the vortices and the emission of sound pulses [56–58]. In general, we find that, in 2D, the time scales of injection, diffusion, and lattice crystallization are faster than in 3D. A particular feature that we see in the early-time dynamics of the 2D simulations is the nucleation of vortices with both positive and negative circulation (i.e., with circulation which is inconsistent with the imposed rotation). We notice that some negative vortices originate from localized rarefaction pulses generated from the rough boundary when the bucket is set into rotation. We associate these pulses with Jones-Roberts solitons [59,60], which are low energy/momentum solutions of the 2D GPE. At higher energy/momentum, these solutions become pairs of vortices of opposite sign (also called vortex dipoles in the literature). The conversion of Jones-Roberts solitons into vortex dipoles occurs if the pulse gains energy from the large positive vortex cluster which starts forming in the center of the bucket. Occasionally, the vortices which are parts of a dipole separate and mix with the rest of the vortices. Over time, the vortices of negative circulation are lost from the system, either colliding (hence annihilating) with positive vortices within the bulk, or by exiting the fluid at the bucket’s boundary (effectively annihilating with their images).

V. CONCLUSIONS

In conclusion, we have employed simulations of the Gross-Pitaevskii equation to study the spin-up of a superfluid in a rotating bucket featuring microscopically rough walls. Within this model, we see several key stages of the dynamics. First, vortices are nucleated at the boundary by the flow over the rough features, typically in the form of small U-shaped vortex lines. Secondly, these U-shaped vortices interact strongly and reconnect, creating a transient turbulent state. This becomes increasingly polarized by the imposed rotation until the vortex configuration consists of vortices of the correct orientation extending from the top to the bottom of the bucket. Finally, the vortex lines slowly straighten and arrange themselves in the expected final vortex lattice configuration. Our results highlight the importance of vortex reconnections [61]: It is generally assumed that vortex reconnections are important in turbulence, but here we have seen that reconnections are essential to create, starting from potential flow, something as simple as solid-body rotation (the vortex lattice). The addition of a single large protuberance or one additional remanent vortex line does not change the dynamics significantly, only speeding up or slowing down the injection of vorticity. Moreover, analogous dynamics arise in the 2D limit.

We reiterate that the GPE is not a quantitatively accurate model of superfluid helium and these results should be interpreted qualitatively only. For example, the role of friction is introduced into the GPE through a widely used phenomenological dissipation term; however, a more accurate physical model of this stage of the dynamics would be provided by the VFM. Also, a distinctive physical property of superfluid helium is its strong nonlocal interactions. This, for instance, supports a roton minimum in its excitation spectrum. While this is absent from the GPE model we have employed, it can be introduced through an additional nonlocal term [62,63]. It would be interesting to see if this causes any significant departures from the dynamics we have reported.

ACKNOWLEDGMENT

N.P., L.G., and C.F.B. acknowledge support from the Engineering and Physical Sciences Research Council (Grant No. EP/R005192/1).

- [1] J. F. Annett, *Superconductivity, Superfluids and Condensates* (Oxford University Press, Oxford, 2004).
- [2] C. F. Barenghi and N. G. Parker, *A Primer on Quantum Fluids* (Springer, Berlin, 2016).
- [3] E. J. Yarmchuk, M. J. V. Gordon, and R. E. Packard, *Phys. Rev. Lett.* **43**, 214 (1979).
- [4] G. P. Bewley, D. P. Lathrop, and K. R. Sreenivasan, *Nature (London)* **441**, 588 (2006).
- [5] K. W. Madison, F. Chevy, W. Wohlleben, and J. Dalibard, *J. Mod. Opt.* **47**, 2715 (2000).
- [6] J. R. Abo-Shaer, C. Raman, J. M. Vogels, and W. Ketterle, *Science* **292**, 476 (2001).
- [7] D. S. Tsakadze, *Sov. Phys. JETP* **19**, 110 (1964).
- [8] C. Josslerand, *Chaos* **14**, 875 (2004).
- [9] K. Kasamatsu, M. Tsubota, and M. Ueda, *Phys. Rev. A* **66**, 053606 (2002).
- [10] U. R. Fischer and G. Baym, *Phys. Rev. Lett.* **90**, 140402 (2003).
- [11] G. M. Kavoulakis and G. Baym, *New J. Phys.* **5**, 51 (2003).
- [12] P. Engels, I. Coddington, P. C. Haljan, V. Schweikhard, and E. A. Cornell, *Phys. Rev. Lett.* **90**, 170405 (2003).
- [13] K. W. Schwarz, *Phys. Rev. Lett.* **64**, 1130 (1990).
- [14] N. Hashimoto, R. Goto, H. Yano, K. Obara, O. Ishikawa, and T. Hata, *Phys. Rev. B* **76**, 020504(R) (2007).
- [15] D. E. Zmeev, F. Pakpour, P. M. Walmsley, A. I. Golov, W. Guo, D. N. McKinsey, G. G. Ihas, P. V. E. McClintock, S. N. Fisher, and W. F. Vinen, *Phys. Rev. Lett.* **110**, 175303 (2013).
- [16] D. Duda, P. Švančara, M. La Mantia, M. Rotter, and L. Skrbek, *Phys. Rev. B* **92**, 064519 (2015).
- [17] A. L. Fetter, *Phys. Rev.* **152**, 183 (1966).
- [18] D. Stauffer and A. L. Fetter, *Phys. Rev.* **168**, 156 (1968).
- [19] G. W. Stagg, N. G. Parker, and C. F. Barenghi, *Phys. Rev. Lett.* **118**, 135301 (2017).
- [20] C. M. Muirhead, W. F. Vinen, and R. J. Donnelly, *Philos. Trans. R. Soc. Lond. A* **311**, 433 (1984).
- [21] P. V. E. McClintock and R. M. Bowley, in *Progress in Low Temperature Physics* (Elsevier, Amsterdam, 1995), Vol. 14, pp. 1–68.
- [22] N. G. Berloff and P. H. Roberts, *Phys. Lett. A* **274**, 69 (2000).
- [23] T. Winiecki and C. S. Adams, *Europhys. Lett.* **52**, 257 (2000).
- [24] A. Vilhois and H. Salman, *Phys. Rev. B* **97**, 094507 (2018).
- [25] K. W. Schwarz, *Phys. Rev. B* **38**, 2398 (1988).
- [26] K. W. Schwarz, *Phys. Rev. B* **31**, 5782 (1985).
- [27] M. Tsubota and S. Maekawa, *Phys. Rev. B* **47**, 12040 (1993).
- [28] K. W. Schwarz, *Phys. Rev. A* **10**, 2306 (1974).
- [29] D. Kivotides, C. F. Barenghi, and Y. A. Sergeev, *J. Low Temp. Phys.* **144**, 121 (2006).
- [30] R. Hänninen and A. W. Baggaley, *Proc. Natl. Acad. Sci. USA* **111**, 4667 (2014).
- [31] R. Hänninen, A. Mitani, and M. Tsubota, *J. Low Temp. Phys.* **138**, 589 (2005).
- [32] L. Pitaevskii and S. Stringari, *Bose-Einstein Condensation* (Oxford University Press, Oxford, 2003).
- [33] S. Choi, S. A. Morgan, and K. Burnett, *Phys. Rev. A* **57**, 4057 (1998).
- [34] M. Tsubota, K. Kasamatsu, and M. Ueda, *Phys. Rev. A* **65**, 023603 (2002).
- [35] B. B. Mandelbrot and J. W. Van Ness, *SIAM Rev.* **10**, 422 (1968),
- [36] B. B. Mandelbrot, *Phys. Scr.* **32**, 257 (1985).
- [37] A. Majumdar and B. Bhushan, *J. Tribol.* **112**, 205 (1990).
- [38] G. R. Dennis, J. J. Hope, and M. T. Johnsson, *Comput. Phys. Commun.* **184**, 201 (2013).
- [39] A. Vilhois, G. Krstulovic, D. Proment, and H. Salman, *J. Phys. A: Math. Theor.* **49**, 415502 (2016).
- [40] See Supplemental Material at <http://link.aps.org/supplemental/10.1103/PhysRevB.102.144520> for movies, `movie_ref` (3D view) and `movie_2d_midslice`.
- [41] T. Frisch, Y. Pomeau, and S. Rica, *Phys. Rev. Lett.* **69**, 1644 (1992).
- [42] G. W. Stagg, N. G. Parker, and C. F. Barenghi, *J. Phys. B: At. Mol. Opt. Phys.* **47**, 095304 (2014).
- [43] A. Aftalion and I. Danaila, *Phys. Rev. A* **68**, 023603 (2003).
- [44] E. Rickinson, C. F. Barenghi, Y. A. Sergeev, and A. W. Baggaley, *Phys. Rev. B* **101**, 134519 (2020).
- [45] T. Kanai, W. Guo, and M. Tsubota, *Phys. Rev. A* **97**, 013612 (2018).
- [46] T. Kanai, W. Guo, M. Tsubota, and D. Jin, *Phys. Rev. Lett.* **124**, 105302 (2020).
- [47] L. J. Campbell and R. M. Ziff, *Phys. Rev. B* **20**, 1886 (1979).
- [48] T. S. Wood, M. Mesgarnezhad, G. W. Stagg, and C. F. Barenghi, *Phys. Rev. B* **100**, 024505 (2019).
- [49] P. Mathieu, J. C. Marechal, and Y. Simon, *Phys. Rev. B* **22**, 4293 (1980).
- [50] J. A. Northby and R. J. Donnelly, *Phys. Rev. Lett.* **25**, 214 (1970).
- [51] D. S. Shenk and J. B. Mehl, *Phys. Rev. Lett.* **27**, 1703 (1971).
- [52] See Supplemental Material at <http://link.aps.org/supplemental/10.1103/PhysRevB.102.144520> for movie, `movie_gaussian`.
- [53] See Supplemental Material at <http://link.aps.org/supplemental/10.1103/PhysRevB.102.144520> for movie, `movie_pos_remnant`.
- [54] See Supplemental Material at <http://link.aps.org/supplemental/10.1103/PhysRevB.102.144520> for movie, `movie_neg_remnant`.
- [55] See Supplemental Material at <http://link.aps.org/supplemental/10.1103/PhysRevB.102.144520> for movie, `movie_2d_large_bucket`.
- [56] W. J. Kwon, G. Moon, J.-Y. Choi, S. W. Seo, and Y.-i. Shin, *Phys. Rev. A* **90**, 063627 (2014).
- [57] G. W. Stagg, A. J. Allen, N. G. Parker, and C. F. Barenghi, *Phys. Rev. A* **91**, 013612 (2015).
- [58] A. J. Groszek, T. P. Simula, D. M. Paganin, and K. Helmerson, *Phys. Rev. A* **93**, 043614 (2016).
- [59] C. A. Jones and P. H. Roberts, *J. Phys. A: Math. Gen.* **15**, 2599 (1982).
- [60] S. Tsuchiya, F. Dalfovo, and L. Pitaevskii, *Phys. Rev. A* **77**, 045601 (2008).
- [61] L. Galantucci, A. W. Baggaley, N. G. Parker, and C. F. Barenghi, *Proc. Natl. Acad. Sci. USA* **116**, 12204 (2019).
- [62] N. Berloff, M. Brachet, and N. P. Proukakis, *Proc. Natl. Acad. Sci. USA* **111**, 4675 (2014).
- [63] J. Reneuve, J. Salort, and L. Chevillard, *Phys. Rev. Fluids* **3**, 114602 (2018).